Helium-induced morphology evolution in tungsten under thermal treatment

Mykola Ialovega, Elodie Bernard, Marie-France Barthe, Régis Bisson, Andrea Campos, Martiane Cabié, Thomas Neisius, Ryuichi Sakamoto, Arkadi Kreter, Christian Grisolia, et al.

To cite this version:

Mykola Ialovega, Elodie Bernard, Marie-France Barthe, Régis Bisson, Andrea Campos, et al.. Helium-induced morphology evolution in tungsten under thermal treatment. Nuclear Fusion, 2022, 62 (12), pp.126022. 10.1088/1741-4326/ac94e3 . hal-03858986

HAL Id: hal-03858986

https://hal.science/hal-03858986

Submitted on 18 Nov 2022

Helium-induced morphology evolution in tungsten under thermal treatment

Mykola Ialovega[a,b,c], **Elodie Bernard**[a], **Marie-France Barthe**[d], **Régis Bisson**[b], **Andrea Campos**[e], **Martiane Cabié**[e], **Thomas Neisius**[e], **Ryuichi Sakamoto**[f], **Arkadi Kreter**[g], **Christian Grisolia**[a], **Thierry Angot**[b], **Celine Martin**[b]

[a]CEA, IRFM, F-13108 Saint Paul-lez-Durance, France
[b]Aix Marseille Univ., CNRS, PIIM, UMR 7345, 13013 Marseille, France
[c]University of Wisconsin-Madison, Department of Engineering Physics, 3DPSI, 1500 Engineering Drive, 53706 Madison, WI, USA
[d]Orleans Univ., CNRS, CEMHTI, 45071 Orleans, France
[e]Aix Marseille Univ., CNRS, Centrale Marseille, FSCM (FR1739), CP2M, 13397 Marseille, France
[f]National Institute for Fusion Science, Toki, 509-5292 Gifu, Japan
[g]Forschungszentrum Jülich GmbH, IEK-4, 52425 Jülich, Germany

E-mail: `celine.martin@univ-amu.fr`

June 2022

Abstract. Surface and near-surface morphology evolution of helium-irradiated tungsten due to thermal cycling up to the ITER-relevant temperature of 1350 K was studied using electron microscopy and positron annihilation spectroscopy techniques. Holes at the surface and bubbles in the near-surface of recrystallized polycrystalline tungsten samples were created by 75 eV helium plasma irradiation with the fluence of $3 \times 10^{23}\,\mathrm{He\,m^{-2}}$ at the surface temperature of 1073 K. Subsequent annealing experiments were combined with a detailed electron microscopy analysis to investigate the shape and density changes of holes and helium bubbles with respect to grain orientation. We show that the initially circular holes and round bubbles became faceted upon heating with 1 K/s ramp up to 870 K. Annealing cycles up to 1350 K induced resulted in bubbles removal in the first 5 nm below the surface and surface smoothing. Electron energy loss spectroscopy measurements allowed estimation of helium gas density and pressure inside bubbles. Positron annihilation spectroscopy allowed to investigate the nature of defects and their evolution in the helium-irradiated tungsten with thermal cycling.

Keywords: Tungsten, Helium, bubble, SEM, TEM, EELS, PAS

1. Introduction

The choice of tungsten (W) as plasma-facing material (PFM) for the divertor of ITER fusion experiment is justified by its high melting point, good thermal conductivity, resistance to sputtering and low hydrogen isotopes retention as compared with previously used carbon PFM [1]. The ITER divertor will be subjected to high thermal loads (up to $20\,\mathrm{MW/m^2}$) and intense particle fluxes composed of hydrogen isotopes (HI) and helium (He) ash. In particular, it has been found that accumulation of He in W PFM due to He-seeding, tritium decay or transmutation significantly affects the morphology of W, inducing formation of various surface structures [2, 3] and bulk damages such as crystal defects [4, 5], cavities filled with He gas (so-called helium bubbles) [2, 6] or even a highly porous W "fuzz" structures [7]. He presence in W and the associated structural changes can alter erosion resistance [8], mechanical properties [9] and HI trapping and release mechanisms [10, 11, 12] - major concerns for the divertor. Furthermore, according to the current ITER research plan [13], ITER will demonstrate high confinement mode with He plasma to ensure that nuclear activation of the vacuum vessel components will not take place. Thus, W PFM of ITER will be enriched with He even before the beginning of the Fusion Power Operation phase.

It is expected that the surface temperature at the ITER divertor strike–points will exceed 1000 K during the discharges due to the high heat loading [1] and might drop down to 340 K between the discharges due to the active cooling of the W plasma-facing units. Such thermal cycles may result in an evolution of the He-induced morphological changes in W which in its turn will lead to further material properties modification. As we showed recently [10], thermal cycling above the irradiation temperature of ∼1053 K significantly affects HI retention mechanisms in He-irradiated W resulting in an increase of D retention at low D fluence as compared with pristine W.

The kinetic energy of incident ions in the ITER divertor region is expected to be below the sputtering threshold of 107 eV [14]. The corresponding implantation range of He ions is on the order of several nanometers [15]. Due to the high particle fluxes ($\sim 10^{24}\,\mathrm{ions\,m^{-2}\,s^{-1}}$) [1], the near-surface region of W PFM will be enriched with He where numerous helium bubbles can be formed.

Numerical simulations [16, 17] have shown that the grain orientation of the W surface plays a significant role in helium depth distribution and helium retention. Experimental studies by Sakamoto et al. [2, 3] revealed a formation of undulated surface structures with a periodic arrangement on {111} and {110} grain orientations under low-energy He irradiation for surface temperatures below 1053 K. Additionally, the experimental work of Parish et al. [18] and the modelling work of Hammond et al. [19] showed a formation of several types of faceted surface structures on He-irradiated W depending on the grain orientation: pyramidal structures on {111} surfaces, simple higher-up surfaces on (211) surfaces, sheet-like features on {100} and {110} surfaces. Results suggested that the appearance of the faceted structures is a cumulative effect of forming a low-surface-tension and of overpressurized bubbles bursting whose size and distribution depends on the grain orientation. Recent experimental studies on single crystal W by Fan et al. [20, 21] showed that surface orientation affects the size and depth distribution profile of helium bubbles after irradiation at an energy higher than the threshold energies for sputtering and displacement. Thus, it is important to consider the grain orientation as an another parameter having an impact on the shape, density and distribution of surface and bulk morphological structures of W subjected to He ions especially at the low kinetic energy expected in ITER.

In this work we investigate the density and shape evolution of the He-induced structural changes in W with respect to the grain orientation due to thermal and D implantation cycles. We aim to expand our knowledge on the behaviour of the metal under temperature and He flux conditions relevant to ITER and to give a clearer understanding on the fundamental mechanisms of HI retention in presence of He. The surface and near-surface morphology evolution is investigated by scanning electron microscopy (SEM) and cross-sectional transmission electron microscopy (TEM) techniques respectively. Positron annihilation spectroscopy (PAS) is used to study evolution of voids and defects in the samples. Thermal cycling experiments were performed in a temperature programmed desorption (TPD) setup. Additionally, a set of *in situ* low-energy low-fluence deuterium (D) ion implantation experiments were realised on one of the samples to probe HI retention properties of the He-enriched near-surface layer of W. In this contribution we also aim to study the effect of a low quantity D presence on He bubbles shape evolution as well as to provide an experimental evidence on He gas presence inside the bubbles.

2. Experiment

Five identical polycrystalline tungsten (PCW) samples, named W0, W1, W2, W3 and W3 bis (99.995%, Toho Kinzoku Co. Ltd.), with a square shape of $7 \times 7\,\mathrm{mm}^2$ and thickness of 0.3 mm, a mechanically polished mirror-like surface and recrystallised at 1773 K in vacuum for 2 h were used in these experiments. Re-crystallisation creates a homogeneous grain structure which is helpful for material analysis and removes some of the natural bulk defects capable of trapping incident HI [11]. The W1, W2 and W3 samples were simultaneously irradiated to helium plasma in the linear plasma device PSI–2 (Jülich, Germany) [22]. The typical incident helium kinetic energy was 75 eV that is below the threshold energies for the displacement damage and sputtering of W by He [23]. Before the He exposure, the samples were pre-heated up to 1053 K by a resistive heater installed on the sample carrier under the samples. This temperature is below the threshold temperature for the fuzz formation [2]. During the 13 s plasma exposure in the PSI–2, the heating was turned off as the samples were heated by the plasma itself. A thermographic measurement showed nearly constant temperature of the samples during the exposure. The incident helium flux measured by the reciprocating Langmuir double probe was $2.3 \times 10^{22}\,\mathrm{He\,m^{-2}\,s^{-1}}$ and the total incident fluence was $3 \times 10^{23}\,\mathrm{He\,m^{-2}}$. The sample W3 bis was also irradiated with 75 eV He ions with the total incident fluence of $3 \times 10^{23}\,\mathrm{He\,m^{-2}}$ but at lower flux of $2.9 \times 10^{20}\,\mathrm{He\,m^{-2}\,s^{-1}}$ at 1073 K. Just after the exposure, the samples were cooled down to room temperature (RT) within a few minutes by the water-cooled sample carrier. Oxygen is the main impurity in PSI–2 and is on the order of 0.1% [24]. Detailed information about the layout of the PSI–2 device, its parameters and operational conditions can be found in [22].

After the He plasma exposure, the W2, W3 and W3 bis samples were introduced into the ultra-high vacuum setup CAMITER (Marseille, France) where they were heated with a constant temperature ramp of $1\,\mathrm{K\,s^{-1}}$ up to 870 K and then left to cool down to RT. Then, the W3 and W3 bis samples experienced a further sequence of four D ion implantation/thermal cycling experiments. 500 eV D_2^+ ions were implanted in the centre of the samples on an area of $30\,\mathrm{mm^{-2}}$ at RT before each thermal cycling experiment: the first one at a peak temperature of 1250 K and the last three ones at a peak temperature of 1350 K. The flux of D ions was about $3 \times 10^{15}\,\mathrm{D\,m^{-2}\,s^{-1}}$ corresponding to the incident fluence by the end of each cycle of $4.5 \times 10^{19}\,\mathrm{D\,m^{-2}}$. The implantation range of 500 eV D_2^+ ions in W is ∼15 nm according to SRIM calculations [15] and corresponds to the depth of the maximum density of He bubbles created during He irradiation of the samples.

Surface and near-surface analysis was performed on the W1 sample (after He irradiation), on the W2 sample (after heating up to 870 K) and on the W3 and W3 bis samples (after all D implantation/thermal cycling experiments) in the centre of the sample (i.e., He and D implantation area) and in the corner of the sample (i.e., He implantation area). This allowed to investigate effects of He irradiation and subsequent thermal cycling up to 870 K and up to 1350 K on the material structure evolution as well as the effect of D ion co-implantation.

SEM observations of the surface morphology were performed in a Zeiss GeminiSEM 500 microscope coupled with an EDAX Electron Backscattered Diffraction (EBSD) detector used to determine grain orientations of the polycrystalline samples. In-lens secondary electron detection was employed for imaging at 1 kV. The low voltage acquisition was suitable for surface studies since it increases topographic contrast. EBSD scans were performed at 15 kV.

Thin lamellae for TEM investigations were cut from grains with {100} surface orientation using the focused ion beam (FIB) technique in a FEI Helios 600 nanolab Dual Beam apparatus. For the successful FIB cutting without damage creation in the near-surface layer of the lamellae, SiO and Pt layers were deposited on the surface of the lamellae. Cross-sectional observations of the near-surface region of the samples were realised on the lamellae with the scanning TEM technique at the acceleration voltage of 200 kV in a TEM FEI Titan 80-300 microscope. The Gatan Image Filter Tridiem installed in the microscope allowed Electron Energy Loss Spectra (EELS) acquisition for elemental detection in the material. The energy resolution for EELS measurements was 1 eV under STEM conditions. High-angle annular dark-field (HAADF) images and EELS spectra were acquired on He bubbles to check the presence of trapped helium.

A procedure [25] was developed to analyze the collected SEM images to investigate the size distribution of holes. The ImageJ software [26] was used to identify particles of interest (holes at the surface and bubbles in the near-surface) on several SEM images (a typical surface area covered by an image was $\sim 3.7\mu\mathrm{m}^2$). Firstly, brightness and contrast adjustment of the images was performed. Then, the FFT bandpass filter was used to remove blurring effects and an appropriate threshold was applied to the particles from the background. Area of particles was computed assuming an ellipsoidal shape and the mean diameter is used for the bubbles distribution. A similar analysis was performed on TEM images. To correctly identify bubbles, under- and over- focused TEM images of the same area of the lamella were compared automatically using a numerical code written in Python language. Due to the weak contrast of the TEM images, the number of helium bubbles with diameters less than 3 nm is underestimated in our analysis. Identification of the bubble location with respect to the surface allowed to compute bubble density and size as a function of depth. The error was estimated as the standard deviation from several SEM or TEM images acquired on grains of the same orientation.

The presence of defects and their depth distribution in the W0, W1, W2 and W3 samples were evaluated by PAS which is a non-destructive technique. In this study, a beam of mono-energetic positrons (e^+) with an energy up to 25 keV is used to probe the first 700 nm under the tungsten's surface. When interacting with electrons (e^-) of the material, positrons annihilate and γ–rays are emitted at the energy of around 511 eV [27]. Positrons preferentially annihilate in low electronic density areas such as vacancy-type defects (monovacancies, vacancy clusters, dislocation loops, vacancy-helium clusters) and He bubbles. The γ–ray spectra is characterized using two parameters: S and W. The S parameter represents the positron annihilation fraction with low momentum electrons (mainly valence e^-). The W parameter represents the positron annihilation fraction with high momentum electrons (core e^-). Thus, each annihilation state (i.e., surface, bulk, defect, etc.) is characterized with specific S and W parameters. If a positron is not efficiently trapped in the metal, it can diffuse and be re-emitted from the surface as free positron or bound to an electron to form a positronium. The positronium (e^+e^- bound state) Ps fraction f_{Ps} is another parameter indicating the presence of defects in a metal. The fraction of the Ps emitted from surface (Ps fraction) depends on the concentration of defects. More details on the PAS technique, the measurement system and data analysis can be found in [28].

Note that some annihilation characteristics have been already experimentally determined in tungsten [29]: $S_L = 0.367(4)$ and $W_L = 0.084(5)$ for the perfect lattice, $S_V = 0.417(1)$ and $W_V = 0.057(1)$ for a single vacancy. The annihilation characteristics S_{VNW}, W_{VNW} of vacancy clusters in tungsten are not known but the maximum and minimum values of S and W ever measured in this material are: $S_{Max} = 0.5026$, $W_{Min} = 0.0364$. S_{Max} and W_{Min} most probably correspond to the annihilation in vacancy clusters V_{NW} with the maximum size detectable with SPB-DB of $N \geq 20$ [30]. The annihilation characteristics S and W as well as the positron lifetime are sensitive to helium trapped in vacancy clusters. Theoretical lifetime of positrons in a cluster V_NHe_n with $n = 6$ He atoms decreases from around 272 to about 140 ps when the number of He atoms trapped in the cluster increases to $n = 10$ [31]. It was also observed that the low momentum annihilation fraction S decreases and W increases in neutron and He-irradiated Nickel due to He trapping in vacancy clusters [32].

3. Results

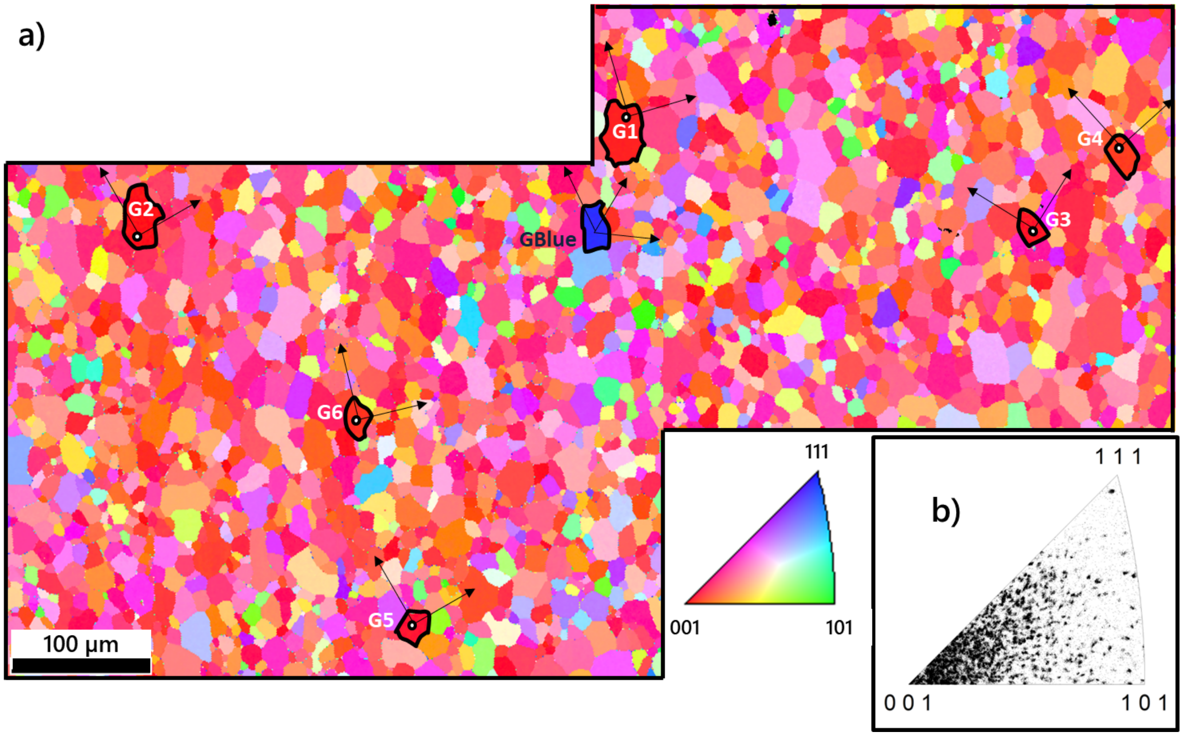

Figure 1. a) EBSD mapping of the PCW sample W1 (after He irradiation) showing several outlined grains of interest. The sets of three arrows indicate projected ⟨100⟩ directions on each grain surface (an arrow pointing upwards is presented as a circle). b) Occurrence (density) of grain orientations in the EBSD map.

3.1. Surface morphology observations

Figure 1 shows the polycristalline W surface analysis using EBSD technique. Grain sizes are about few tens of μm for the larger ones (figure 1 a) and the nearly-{100} orientation of the grains (red color) is dominant (figure 1 b). There is no clear relation between the orientation and the grain size. A similar texture was observed on all the samples used in the study (large grain sizes and dominant {100} orientation) induced by the recrystallisation [33] of the pristine samples. Several grains of interest with {100} and {111} orientations were then selected on all samples for the morphological analysis (e.g., grains G1-G6 with {100} orientation, grain GBlue with {111} orientation on the W1 samples surface are outlined in figure 1 a).

Figure 2 a (resp. figure 2 d) shows a typical SEM image of {100} surfaces (resp. of {111} surfaces) of the W1 sample featuring holes (black dots) and some

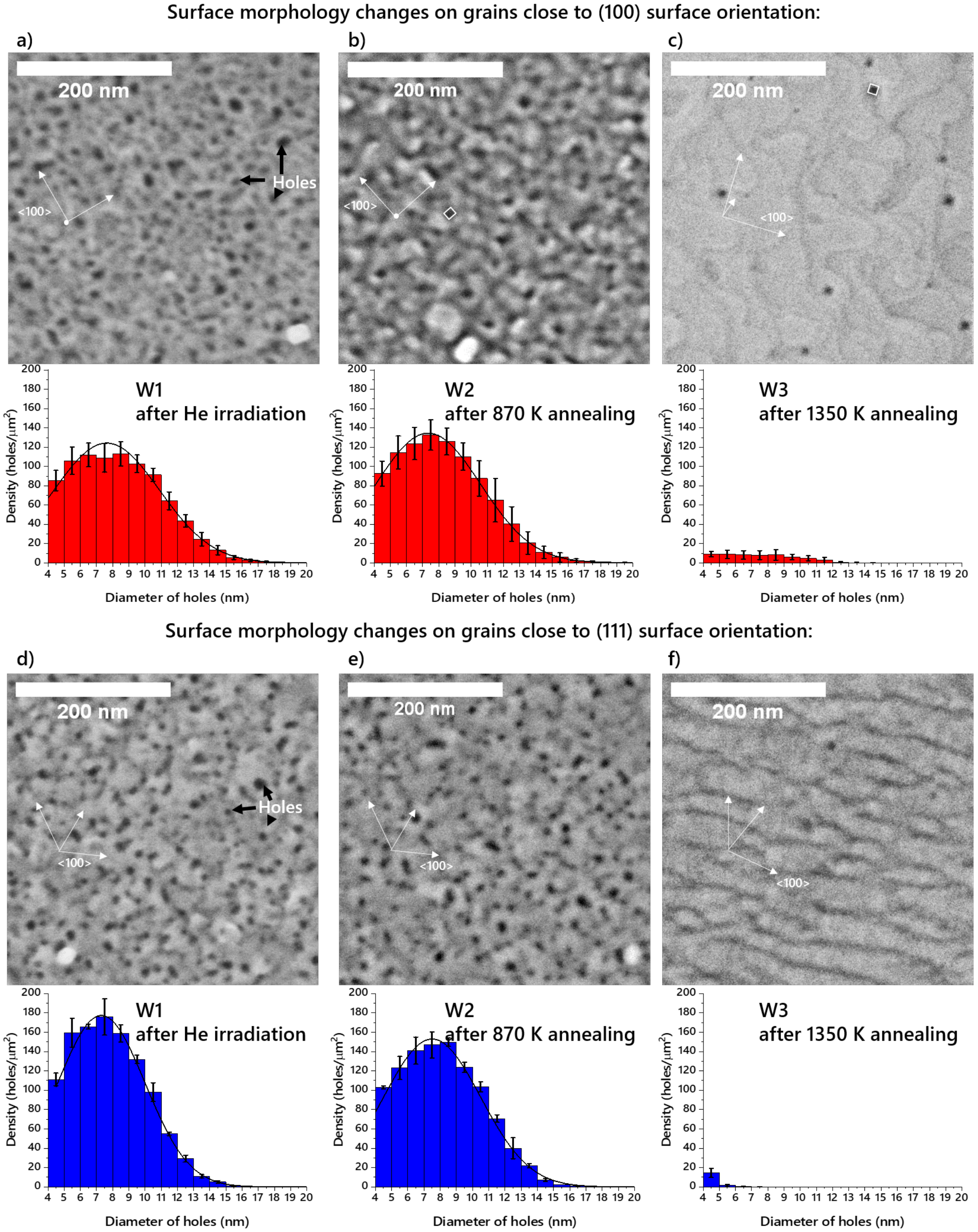

Figure 2. SEM images of {100} (resp. {111}) tungsten surface and the corresponding distribution function of the holes (black dots in SEM images): (a) (resp. d) after He irradiation (W3), (b) (resp. e) after the first annealing up to 870 K (W2) and (c) (resp. f) after the thermal cycling experiments up to 1350 K (W3). The sets of three arrows indicate projected ⟨100⟩ directions on the grain surface.

nanostructures (white dots) which are rather irregularities of the surface than redeposited W dust particles since their edges are aligned with crystallographic directions of the substrate. The shape of the holes on all grains was found to be close to circular with diameter up to ∼18 nm. The size distribution of the holes is Gaussian-like centered at $7.5 \pm 3\,\mathrm{nm}$. The maximum of the distribution is at 115 ± 15 holes per μm for $\{100\}$ and 175 ± 20 holes per μm for $\{111\}$ surfaces.

SEM analysis performed on the W2 sample's surface after annealing up to 870 K revealed a modification of the shape of the holes from circular to almost square on $\{100\}$ grains with edges parallel to $\langle 100\rangle$ directions (figure 2 b). Within the resolution capability of the SEM images no shape modification of the holes on $\{111\}$ surfaces was found (figure 2 e). The density distribution functions of the holes on $\{100\}$ and $\{111\}$ grains did not change significantly upon heating up to 870 K.

SEM analysis on the W3 sample's surface after the thermal cycling experiments up to 1350 K revealed an annealing effect of the TPD ramps on the surface morphology: the number of holes decreased by a factor of 10 on $\{100\}$ and $\{111\}$ grains (figures 2 c and 2 f respectively). The shape of the remaining square holes on $\{100\}$ grains did not change. No difference was found between the shape of the holes in He and D co-implanted central area of the sample and He-only-irradiated area in the corners of the sample revealing that D implantation in our experimental conditions does not play a role on the surface morphology modification.

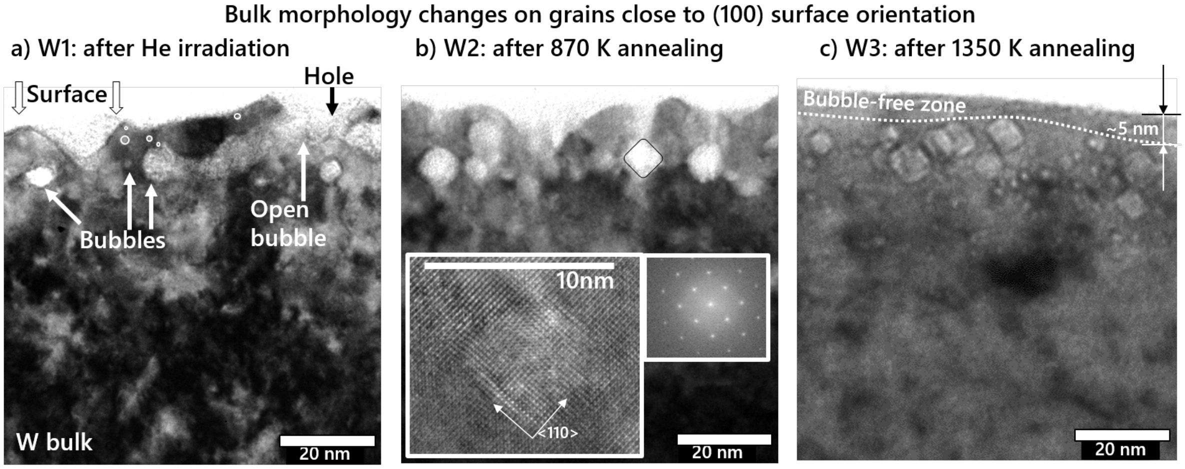

Figure 3. Cross-sectional TEM images of the near-surface region of tungsten: (a) after He irradiation (W1), (b) after the first annealing up to 870 K (W2) and (c) after the thermal cycling experiments up to 1350 K (W3). In (b) a faceted bubble is outlined and the inset shows HRTEM image on another faceted bubble and the corresponding FFT pattern.

3.2. Near-surface morphology observations

Figure 3 shows TEM bright-field images of lamellae cut on $\{100\}$ grains of the W1, W2 and W3 samples. The images were acquired with orientation near [001] zone axis. He irradiation caused formation of a significantly damaged 20 nm thick near-surface layer in tungsten, with presence of numerous He bubbles of different size in the layer (figure 3 a). Majority of the smallest bubbles with diameters $d < 3\,\mathrm{nm}$ are found just below the surface, but they are observed up to ∼100 nm deep. Larger bubbles are preferentially located within $10-20$ nm layer below the surface (figures 3 a). Observed by TEM in zone axis (ZA) of [100] direction, the bubbles seem to have a shape close to round. Furthermore, our observations evidence that the holes at the surface observed with SEM are open He bubbles located close to the surface. This experimental observation confirms the findings of molecular dynamics (MD) simulations by Sefta et al. [34] which predicted the bursting behaviour of subsurface overpressurized helium bubbles.

Initial annealing up to 870 K on the W2 sample did not change the bubble density in the near-surface (figure 3 b). However, the shape of some He bubbles evolved: they appear faceted as squares with round corners and edges parallel to $\langle 110\rangle$ directions as presented in the high-resolution TEM (HRTEM) image in inset of figure 3 b. The FFT spectrum of the image exhibits a spot pattern indicating that the lamella is a single crystal W without presence of a large number of crystal defects. Note that He outgassing of about $3.6\times10^{18}\,\mathrm{He\,m^{-2}}$ is observed during the initial annealing to 870 K [10], which may be related to the He bubbles reshaping.

The further set of four thermal cycling experiments up to 1350 K on the W3 sample induced a remarkable change in the microstructure of He-irradiated W (see figure 3 c). There are no more bubbles within a 5 nm subsurface layer (bubble-free zone) of the sample. Annealing of the open bubbles resulted in the surface smoothing as was evidenced with SEM at the surface (figure 2 c and f). All remaining bubbles in the near-surface appear faceted as squares independently on the bubble size. Lamella was then tilted to observe bubble shapes in different ZA. Figure 4 a shows helium bubbles having a square shape with edges parallel to $\langle 110\rangle$ directions when observed in ZA of [100] or shaped close to hexagons when observed in ZA of [110] and [111] in samples W3 and W3 bis. The total amount of He outgassed from the W3 sample during all thermal cycles is $2.7\times10^{19}\,\mathrm{He\,m^{-2}}$ or less than 0.01% of the incident helium irradiation fluence [10] suggesting that a significant amount of He remained in the sample.

3.3. EELS analysis on helium bubbles

EELS spectrum presented in figure 5 was acquired at 1 μm away from the surface of the lamella cut from the W2 sample, thus, in the pristine bulk part of the sample which was not affected by He irradiation. The spectra feature typical bulk W plasmon EELS spectra with the main peak at 25 eV [35]. An increase of W thickness results in the increase of the plasmon peaks intensity while the position and width of the peaks remain the same. Note, that the measurements were realized on the samples W2 and the thickness of tungsten was computed using the model by Iakoubovskii et al. [36].

Figure 6 presents HAADF images featuring bubbles (dark areas), W crystal (bright area) and red dots which indicate locations where STEM-EELS spectra were acquired. W bulk spectra (black lines in STEM-EELS figures) were acquired 1 μm deep from the surface. Note that, since position and width of the peak remains same in all three samples W1, W2 and W3, thermal treatment did not affect the bulk part of the helium-

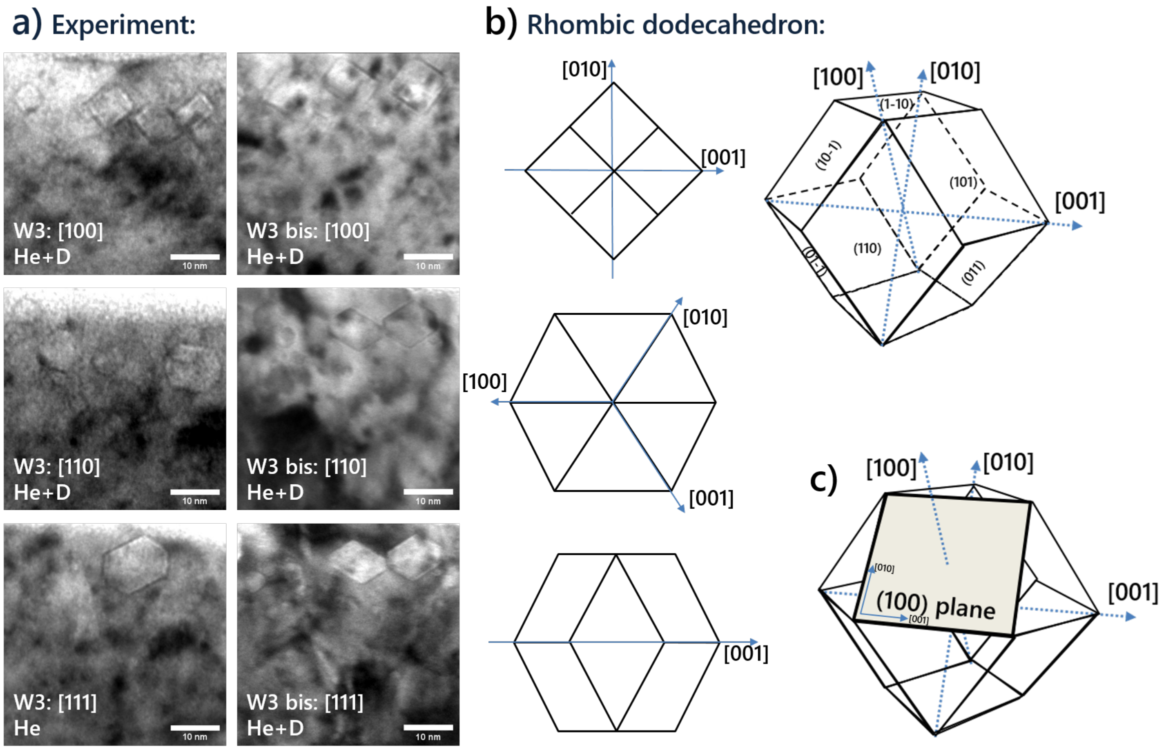

Figure 4. (a) TEM images of He bubbles in tungsten (samples W3 and W3 bis) in [100], [111] and [110] zone axis in He and He+D implantation area. (b) Schematic representation of a rhombic dodecahedron with its projections in [100], [111] and [110] zone axis and (c) its truncation with the {100} plane.

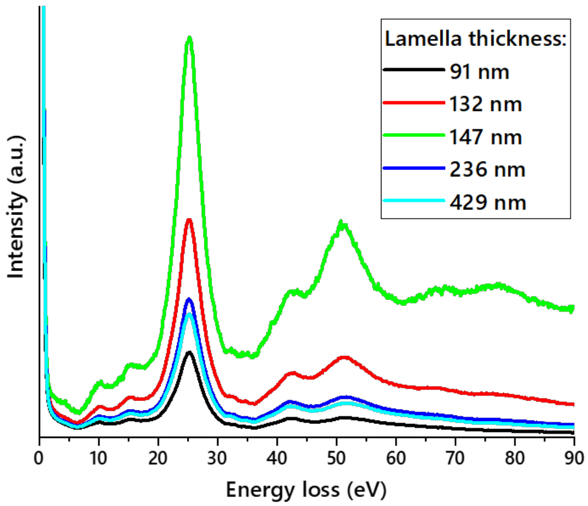

Figure 5. Normalized to the zero-loss peak EELS spectrum shape change as a function of tungsten lamella thickness.

irradiated samples.

Red spectra in figure 6 were acquired close to centre of helium bubbles and feature additional contributions to the bulk W spectra resulting in an increased width and shape

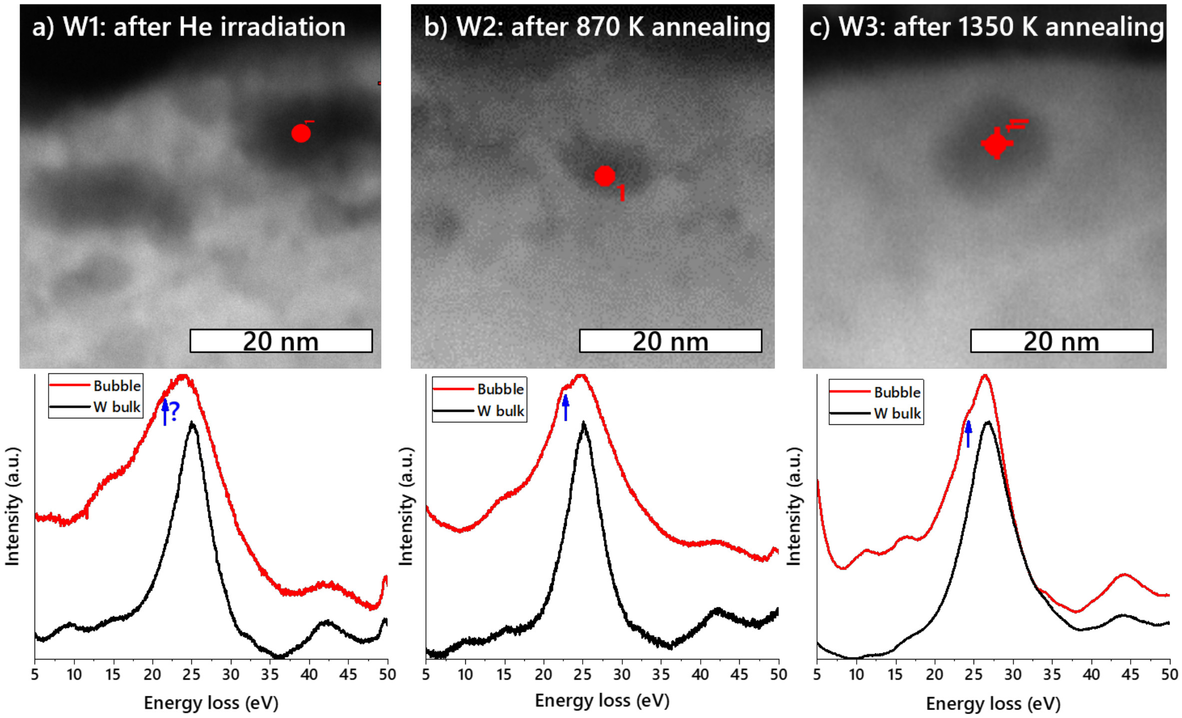

Figure 6. HAADF images (top) and Low-loss STEM-EELS measurements (bottom) on He bubbles and a bulk part of tungsten (a) after He irradiation (W1), (b) after the first annealing up to 870 K (W2) and (c) after the thermal cycling experiments up to 1350 K (W3). Spectra are normalized to the intensity of the W plasmon at 25 eV and red curves are shifted vertically with respect to black curves for clarity.

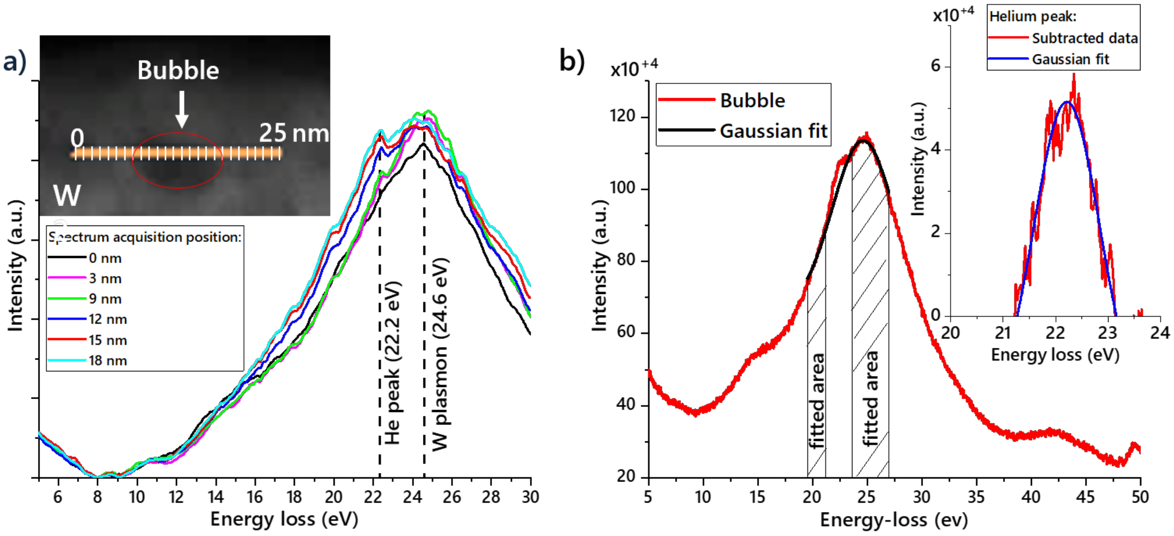

Figure 7. (a) STEM-EELS profile measurements on a He bubble in the sample W2. (b) EELS spectrum acquired from the centre of the bubble and the corresponding Gaussian fit. The inset image represents the extracted He peak fitted with a Gaussian. Spectra are normalized to the zero-loss peak.

evolution of the EELS spectra in the [5,35] eV domain. The width of the red spectrum becomes narrower after the annealing cycles and gets close to width of the black (bulk) spectrum in the sample W3. This indicates a recovery of the helium-induced defects towards the undamaged W crystal. Indeed, the variations of the W plasmon width could be only due to the stress field around He bubbles and to defects created by He irradiation. One can note that contamination of the samples with oxygen which is the main impurity in the PSI–2 plasma may result in a wider EELS spectrum [37]. However, since no oxygen peaks were obtained in our experiments (figure 5), the effect of oxidation can be neglected.

A clearly distinguishable helium peak at around 22 eV is evidenced on bubbles in W2 and W3 samples (figures 6 b and c respectively). The measured helium peak position is "blue" shifted from 21.22 eV which is the energy of $1s^2 \rightarrow 1s2p$ transition of a free He atom [35]. This He peak probably contributes to the red shift of the W plasmon peak which is also visible in the W1 sample. We assume that a shift of the peak in the sample W1 is also caused by the presence of He but the greater width of the W plasmon peak due to the large number of defects and high stress could mask the He peak.

To prove the appearance of the He peak on a bubble, an EELS profile measurement was realised on the sample W2. As shown in figure 7 a, at the position 0 nm the EELS spectrum does not have any He contribution and represents a typical bulk W spectrum. A clear He peak starts to appear at the position ∼9 nm, reaches a maximum intensity at the position ∼15 nm and vanishes at the position ∼21 nm. This indicates that the bubble size might be larger than it appears in the STEM image in figure 7 a or that several bubbles overlap and He contained in them contributes to the profile measurement.

To extract the He peak from the rest of the spectra, the plasmon peak was fitted with Gaussian function [38, 39] in the energy range from 19.5 to 21.2 eV and from 23.6 to 27.1 eV as presented in figure7 b (black curve). He signal is plotted in the inset image and was also modelled using a Gaussian. The energy position of He peak is then given by the position of the Gaussian maximum and is equal to 22.2 eV.

3.4. Positron annihilation spectroscopy measurements

For relevant comparison of the PAS results on the W1, W2 and W3 samples, the reference pristine sample W0 was used. From figure 8 a and b it is noticeable that a strong difference in annihilation characteristic of positrons occurs at the kinetic energy of 2 keV for the W1 and W2 samples (peak in S and a valley in W) while S continuously decreases and W increases respectively for the W0 and W3 samples. In figure 8 c, the S-W curves of the samples W1 and W2 extend more to the upper left corner of the S-W space i.e. they show the highest level of defects while both, the pristine and W3 samples, indicate a better tendency towards the perfect W lattice. Figure 8 d shows that low kinetic energies (< 2 keV) positrons are re-emitted from the surface as positroniums Ps. The higher value of the Ps fraction in the W0 sample in the energy range between 2 and 12 keV is an indication of a lower number of the vacancy type defects comparing

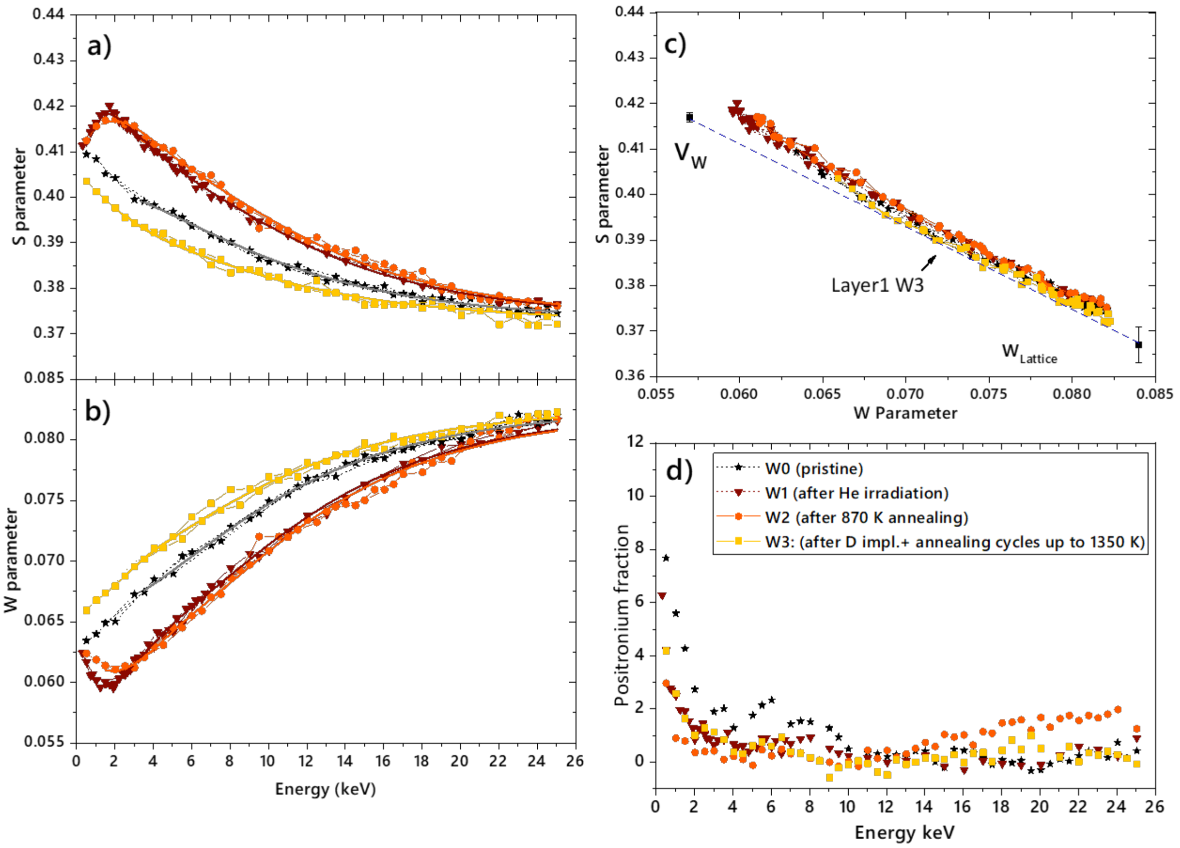

Figure 8. PAS results on the samples W0, W1, W2, W3: evolution of the normalized (a) S and (b) W parameters with the positron kinetic energy (solid lines show fit of the data with VEPFIT [40]); (c) S and W parameters dependence; (d) positronium fraction versus positron kinetic energy.

with the samples W1, W2 and W3.

4. Discussion

4.1. Helium-induced formation of surface holes

Holes and bubbles are well known to be formed onto the surface of W with energy below the sputtering threshold and with high He fluence above 10^{23} He/m^2 [2, 41, 42]. In our experiments, formation of holes on the W surface after 75 eV/He plasma exposure at 1053 K clearly can not be due to the simple sputtering since the kinetic energy of He ions was below the sputtering threshold of 105 eV [23]). Also, only about 60% of W atoms of the first surface plane were sputtered by oxygen impurities present in the PSI–2 plasma. Our TEM observations (figure 3) showing a high density of large bubbles near the surface confirm that holes are open helium bubbles which presumably bursted according to the mechanism described by MD simulations of Sefta et al. [34].

During irradiation, He atoms start to accumulate in W in interstitial positions where they tend to form small helium clusters (so-called self-trapping mechanism) [4, 43, 44].

When the number of He atoms in the cluster exceeds a temperature-dependent threshold (6 to 9 He atoms in the cluster), the pressure in the cluster is reduced by creating a Frenkel pair (a vacancy and a self-interstitial W atom) [45, 46]. This process is called a trap mutation mechanism. Small mobile clusters are not thermally stable at high temperatures (e.g., during He irradiation or the thermal cycling) and can contribute to the other He-vacancy clusters forming He bubbles [46, 47]. Helium accumulation inside the bubbles may result in bubble growth towards the free surface. The overpressurized bubbles located close to the surface may undergo pressure relief via bursting resulting in surface cratering (holes formation) and He release. Bursting of the pressurized bubbles with mean diameter $\sim 7\,\mathrm{nm}$ in the subsurface layer of our samples (figure 2) results in a zero density of bubbles for depths lower than 7 nm. A maximum density is then measured at 10-15 nm in depth (figure 9) which is in a good agreement with the numerical simulations using finite element method performed by Delaporte-Mathurin et al. [46].

Furthermore, surface orientation shows an effect on depth distribution of He and on size of He bubbles [16]. Greater implantation depth of He is expected on {111} tungsten surface due to the channeling effect [20, 21]. In our case, there is no effect of orientation on the mean size of the holes at the surface of the sample W1 (figure 2) suggesting that the mean size of bubbles in depth is similar for {100} and {111} surface orientations. This may be due to the low kinetic energy of the incident He ions for which the channeling effect is negligible [48]. However, there is a difference in the number of holes at the {100} and {111} surfaces of about 20% which is probably related to a different He bubbles density and different energy barrier for bubbles bursting. On one hand, the displacement energy in W is minimal for ⟨100⟩ direction and maximal for ⟨111⟩ [49] direction. Thus, if initially He bubbles are distributed equally in the near-surface layer of {100} and {111} grains, less bubbles will be able to burst on {111} surface. On the other hand, the elevated temperature of the sample of 1053 K during irradiation induces high diffusion of helium and defects in specific directions on different grains resulting in a variation of surface holes and He bubbles density. MD simulations by Hammond and Wirth [16] suggest much higher He concentration below {111} tungsten crystallographic surface due to the favorable formation of adatom/substitutional helium pairs even by a single helium interstitial. High concentration of He clusters under the {111} surface results in the higher density of the ruptured bubbles on {111} surface observed in our samples.

4.2. Shape of helium bubbles and surface holes

One of the main results of our study is that holes and bubbles become faceted due to the annealing cycles. Recent experimental works of El Atwani et al. [50, 51] and Ohno et al. [52] reported bubbles faceting at grain boundaries and in the bulk of He-irradiated tungsten respectively. Also, Dürrschnabel et al. [53] found faceted voids in neutron-irradiated W in which He might be aggregated due to transmutation of impurities.

The previous studies about bubbles in metals highlighted that, firstly, shape of

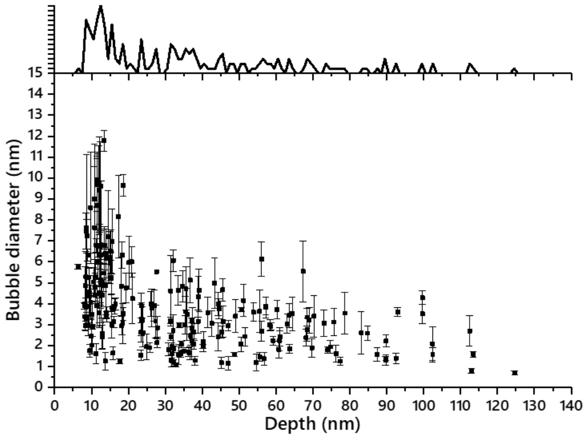

Figure 9. Depth distribution of helium bubbles in W irradiated with 75 eV He ions at 1053 K and a total incident fluence of 3×10^{23} He m^{-2} (error bars are the difference of the major and minor diameters).

the bubbles is determined by the lattice where anisotropic elastic stress dominates [54]. Secondly, bubbles in bcc metals hold uniaxial polyhedral shapes [54]. Thirdly, formation of the faceted bubbles is favourable in terms of the gas/metal system energy: facets are developed due to the tendency to minimize the overall free energy of the system [55]. The free energy of helium gas, the internal energy of W matrix without the bubble, the elastic energy and the free energy of the bubble surface contribute to the system energy. A change of the total energy of the system depends on the shape and volume of the bubble, gas pressure and surface energy [54, 55]. At equilibrium, the surface energy of a bubble is compensated by its internal pressure [56]. Thus, the reduction of the total energy of the system would lead to a development of low-energy facets in preference to a spherical shape which has a higher energy. This requirement is satisfied when the lattice around the bubbles rearranges its surfaces with surface diffusion of atoms and vacancies and, hence, facets are formed.

Finally, in bcc metals, {100}, {110} and {111} faces have the lowest surface energy since the surface energy of a crystallographic plane depends on its planar density. The planar density in W crystal is greater for {110} face and, thus, the surface energy is the lowest for {110} than that of the other faces. This considerations bring us to the conclusion that the voids in W would form faces of {110}.

Our TEM observations of the bubbles in different zone axis in the samples W3 and W3 bis (figure 4 a) allow to narrow down the real 3D shape of the bubbles in W to 3 polyhedron shapes: an octahedron, a cuboctahedron and a rhombic dodecahedron (RhD). RhD has 12 congruent rhombic faces of {110} where every face is a parallelogram delimited by ⟨110⟩ edges. We suggest that RhD (figure 4 b) is the real 3D structure of helium bubbles in W. Firstly, the observed [100] ZA square shape with edges parallel to ⟨110⟩ directions can only be attributed to the RhD shape. Also, hexagon-like shape is observed in [110] ZA that is also the projection of RhD. The difference between the experimentally observed shapes and the projections of RhD in [110] and [111] ZA might be due to the slight tilt of the lamella away from the ZA for easier bubbles observation. Secondly, truncation of the RhD shape with $\{100\}$ plane results in a square shape with edges parallel to $\langle 100\rangle$ directions as shown in figure 4 c. This could be an explanation for the SEM observations of square holes on the W2 and W3 surfaces after the corresponding annealing cycles (figure 2). Thirdly, while octahedron-shaped He bubbles were reported previously for fcc crystals [54], theoretical modelling of He atomic configuration in a bcc crystal showed that helium bubbles form a perfect RhD shape [57].

Lastly, our TEM observations of lamellae cut from He irradiated (corner) and He/D irradiated (centre) areas of the sample W3 revealed no difference in the size, density and shape of helium bubbles after the implantation/TPD experiments. This suggests that the presence of minute amount of D does not play a role in the morphology changes of He-irradiated W. Also, the difference in the incident He flux experienced by the samples W3 and W3 bis was not found to play a role in bubbles shaping.

4.3. Density and gas pressure in helium bubbles

Though there was no experimental results about helium density and pressure in bubbles in tungsten up to now, previous numerical studies of He bubbles formation in W and experimental works on various metals have shown the following trends:

Firstly, bubble size is inversely related with pressure [39]. It is proposed that the initial step of bubble formation is the diffusion and agglomeration of vacancies with several He atoms trapped [19, 46]. Considering that a maximum of 6 He atoms can be accommodated in a single vacancy, the maximum He density for bubbles in W can be estimated as $6/\Omega = 373\,\mathrm{nm}^{-3}$, where $\Omega = 1.6079\times10^{-2}\,\mathrm{nm}^{-3}$ is the atomic volume of W. Several works [38, 39, 58, 59] estimated He density in bubbles in different metals reaching up to to $200\,\mathrm{nm}^{-3}$ (see figure 10 a). These values seem to be high when compared to the density of liquid He ($20\,\mathrm{nm}^{-3}$ at 4 K and 1 bar).

Secondly, due to the effect of the short-range Pauli repulsion coming from wave function overlap in neighbouring atoms, high density of He in bubbles can result in an energy blue shift of the He K-edge ($\Delta E = 0.5 - 3\,\mathrm{eV}$) with respect to its value of 21.218 for the free He atom [39]. Thus, ΔE indicates internal gas pressure and varies almost linearly with He density n independently on the surrounding material: $\Delta E \approx C\,n$.

The gas pressure is an important parameter which influences faceting of the bubbles, their growth and ability to move as well as to retain hydrogen isotopes. The gas density n inside helium bubbles is directly related with pressure and can be calculated using quantities experimentally measured by the HAADF-EELS technique. n is related to the unscattered beam intensity I_z ("zero-loss" peak composed by the electrons that pass through the metal without interaction), the intensity of the helium K-edge $1s \rightarrow 2p$ transition I_p and the bubble diameter d according to the following equation [58]:

$$n = \frac{1}{\sigma_{2p}}\frac{I_p}{I_z d}, \qquad (1)$$

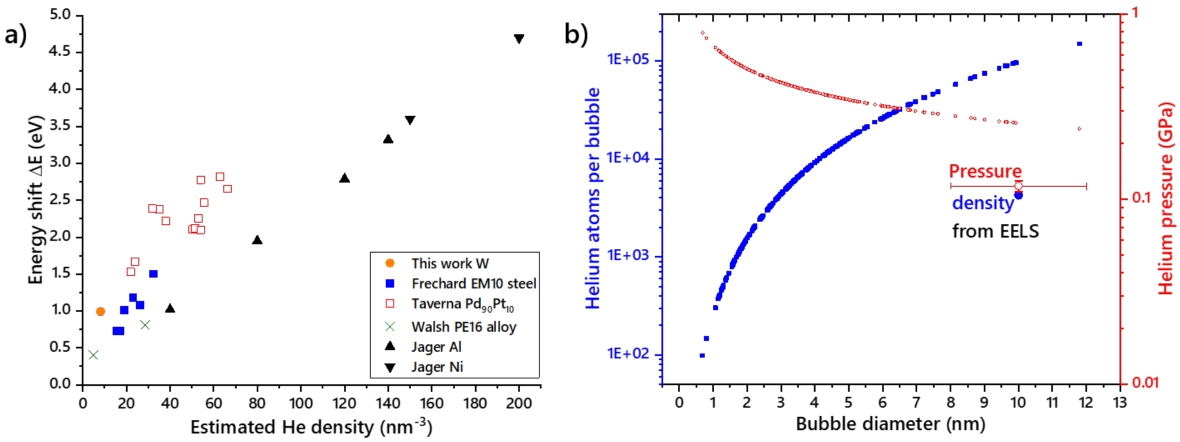

Figure 10. (a) Measured energy shift as a function of estimated He density in bubbles in different materials using data reported by Taverna [38], Frechard [39], Walsh [58] and Jager [59]. (b) Estimated helium content using an empirical relation [19] (blue curve and left axis) and the corresponding pressure in helium bubbles (red curve and right axis) versus the bubble's diameter. The two colored points denote the density and pressure estimated using EELS measurements. The error bars represent the standard errors.

where the inelastic scattering cross-section σ_{2p} is dependent on the He density in the bubbles itself and has to be calculated using delocalized wave functions [60].

There are several factors which hamper the He detection in bubbles in W with the EELS technique. Firstly, the bubble of interest in the sufficiently thin lamella should not be damaged by the preparation process and contain sufficient amount of He gas. Secondly, He peak may appear shifted towards the W plasmon in the overpressurized bubbles [39, 61, 58]. Lastly, a presence of impurities such as oxygen in the substrate (e.g., oxidation) or inside the bubble may add another contributions to the spectrum [53].

The EELS spectrum acquired on a round bubble in the sample W1 (figure 6 a) does not feature a distinct He peak. An increase of the width and a difference in shape of the spectrum of the W plasmon signal can be explained by the influence of the stress field around the bubble on the electron beam and a presence of helium peak in the spectra. Thus, the slight "red" shift of the intensity maximum might be associated with the presence of an additional peak and can be an indication of He presence in the bubble.

However, the spectra measured on faceted bubbles after the initial annealing up to 870 K and after the thermal cycling experiments up to 1350 K (figure 6 b and c respectively) feature a distinct additional peak at 22.2 eV which is close to the He edge at 21.2 eV. Furthermore, since all bubbles appear faceted after the thermal cycling experiments, we conclude that the bubbles and W lattice are in thermal equilibrium and, thus, there is no stress field to modify the EELS spectra. These considerations lead us to the conclusion that the additional peak is the "blue" shifted He K-edge by $\Delta E = 0.99$ eV. Also, our results show that He is still present in bubbles after the thermal cycling up to 1350 K, which is consistent with our TPD results [10] and the expected behaviour of He in the metal [61].

For the case of the EELS measurements on the $\sim 10\,\mathrm{nm}$ bubble in the W2 sample presented in figure 7 b, $\frac{I_p}{I_z d} \approx 5.1 \times 10^4\,\mathrm{m}^{-1}$. The lower boundary of the number density can be calculated considering the scattering cross-section for the free helium atom. Using a formula derived by Walsh et al. [58], σ_{2p} is $6.3 \times 10^{-24}\,\mathrm{m}^2$ under our experimental conditions. The estimated He density in the bubble is $8.13 \times 10^{27}\,\mathrm{He\,m}^{-3}$ which is in a good agreement with the experimental data obtained by different authors as presented in figure 10 a.

In general, helium pressure is often estimated using Laplace-Young equation [39] $p = 2\gamma/R$ which describes the pressure as a ratio of bubble radius with the internal pressure. However, the rise in temperature during the initial annealing step leads to a decrease of helium density without affecting bubble's size. Therefore this equation cannot describe the system studied in this paper in a qualitative way.

The other approach relies on the ideal gas law. Considering He implantation at 1053 K, He pressure in the bubble of figure 6 b in W2 sample, of estimated volume $523.6\,\mathrm{nm}^{-3}$ is 0.12 GPa (figure 10 b). Our estimated value of the pressure is close to the value reported by Frechard et al. [39] for the case of the same size He bubble in a martensitic steel where σ_{2p} was also considered to be independent on He density.

Although EELS does not allow direct measurements of He gas pressure in bubbles in a metal, an estimation of the pressure can be also done using the results of MD simulations. Hammond et al. [19] suggested a two-parameter empirical correlation for the number of helium atoms in a bubble, n_{He}, as a function of the number of vacancies, n_V, generated during the bubble formation under 100 eV/He plasma exposure at 933 K which is close to our He irradiation conditions:

$$n_{He} = 5 n_V^{0.86}. \tag{2}$$

The number of vacancies is related to the bubble size. The volume of a spherical bubble is approximately $V = n_V \Omega$, where $\Omega = 1.6079 \times 10^{-29}\,\mathrm{m}^{-3}$ is the atomic volume of W. Thus, the number of He atoms in a bubble with diameter d is:

$$n_{He} = 6.2 \times 10^{24}\,(\pi d^3)^{0.86}. \tag{3}$$

Gas pressure in a bubble can be then estimated using the ideal gas law. Figure 10 b shows the number of helium atoms per bubble and the corresponding gas pressure in the bubbles that would be created under our irradiation conditions. Furthermore, the estimated gas pressure using the empirical relation (3) for n_{He} is in agreement with results of Frechard et al. [39]. On the other hand, MD simulations by Sefta et al. [34] predict the pressure of 10–30 GPa for the case of overpressurized helium bubbles in W indicating that the values presented in our work are probably underestimated. The calculations presented here can be improved by using a more appropriate model linking the He content to the bubble size.

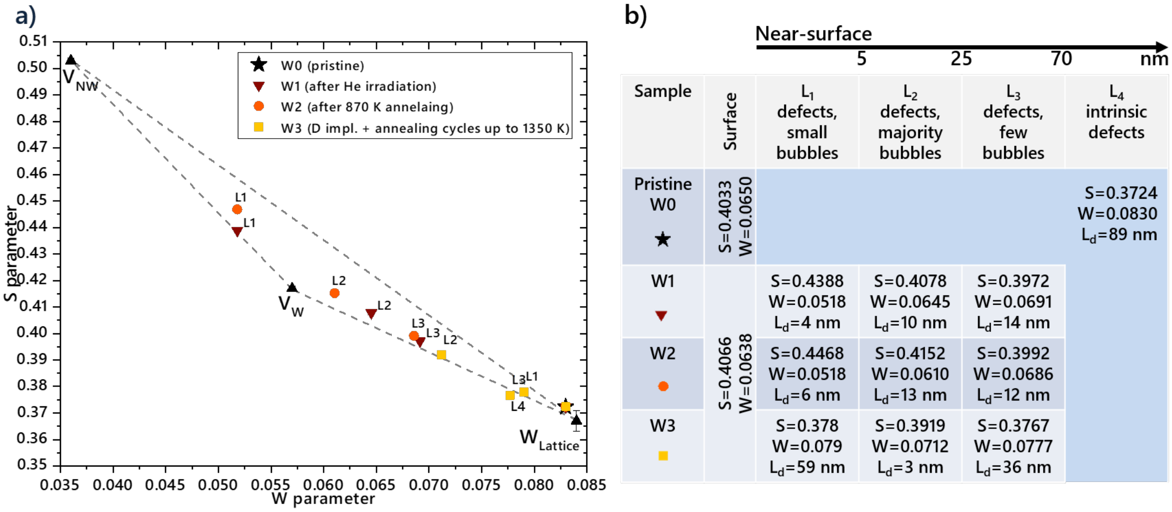

Near-surface
5 25 70 nm

Sample	Surface	L_1 defects, small bubbles	L_2 defects, majority bubbles	L_3 defects, few bubbles	L_4 intrinsic defects
Pristine W0 ★	S=0.4033 W=0.0650				S=0.3724 W=0.0830 L_d=89 nm
W1 ▼	S=0.4066 W=0.0638	S=0.4388 W=0.0518 L_d=4 nm	S=0.4078 W=0.0645 L_d=10 nm	S=0.3972 W=0.0691 L_d=14 nm	
W2 ●		S=0.4468 W=0.0518 L_d=6 nm	S=0.4152 W=0.0610 L_d=13 nm	S=0.3992 W=0.0686 L_d=12 nm	
W3 ■		S=0.378 W=0.079 L_d=59 nm	S=0.3919 W=0.0712 L_d=3 nm	S=0.3767 W=0.0777 L_d=36 nm	

Figure 11. Results of the adjustments of PAS data with VEPFIT for the samples W1, W2, W3 and the pristine PCW sample. (a) S parameter versus W parameter. (b) Summary of the fit parameters for the different layers identified in the near-surface of the samples.

4.4. Depth distribution of defects

The VEPFIT program [40] was used to analyze the depth distribution of defects in the samples. This program solves the positron transport equation taking into account the implantation, diffusion, drift and trapping of positrons in a material. In practice, VEPFIT fits the $S(E)$ and $W(E)$ parameter curves as a function of positron kinetic energy considering physical properties of the material and the Makhovian implantation profiles of the positrons. After imposing appropriate boundary conditions for the surface related processes, the sample can be modelled as a succession of several homogeneous layers of various thickness with different annihilation characteristics S, W and the effective diffusion length L^{+}_{eff} of the positrons. This allows to find the best and reasonable fit for the PAS data based on the near-surface imaging results obtained with TEM.

The results of the fit are presented in figure 11. It has to be noticed that the data for low energy positrons are not taken into account for the fitting, because S and W values include the annihilation of positronium formed at the surface due to epithermal positron backscattering. The energy threshold we use as starting point for fitting depends on the Ps fraction value and its evolution as a function of energy. It can be noticed that the Ps fraction becomes very low when positron energy is equal or larger than 1.5 keV in the irradiated samples (W1, W2 and W3). For the pristine sample, the energy threshold is equal to 2 keV. Starting from 2 keV, the positronium fraction evolution is diffusion dependent and can be correctly modelled by the VEPFIT program. We began by fitting the PAS data collected on the pristine sample W0. The data can be fitted considering that the pristine sample consists of one homogeneous layer. The determined S and W

parameters are close to the perfect W structure (S_L= 0.367(4) and W_L=0.084(5)[29]). The slight difference means that the layer still contains some of the intrinsic defects remaining after annealing at 1773 K for 2 h.
The effective diffusion length is lower than the one found in perfect lattice (135 nm [62]). The concentration of vacancy defects still present in the pristine sample can be estimated considering that the trapping rate of positrons K_D depends on the effective diffusion length as follows:

$$K_d = \lambda_L \left[\left(\frac{L^+}{L^+_{eff}} \right)^2 - 1 \right], \tag{4}$$

where L^+ is the intrinsic diffusion length in perfect tungsten fixed at 135 nm [62] and λ_L is the lattice annihilation rate ($\lambda_L = 1/\tau_L$) with the lattice positron lifetime τ_L of 105 ps [31]. The trapping rate K_d at the detected defects d is the product of their concentration C_d and their specific trapping coefficient μ_d. Considering that the trapping coefficient of single vacancies in tungsten (Z = 74) can be approximated to the value determined for the single vacancy in tantalum (Z = 73, $\mu_V = 6 \pm 3 \times 10^{-15}\,\mathrm{s}^{-1}$ [63]), we estimate the concentration of vacancy defects in the pristine sample at about $2 \times 10^{24}\,\mathrm{m}^{-3}$.

To fit the PAS data for the He-irradiated sample W1, four homogeneous layers have to be introduced: three of them are in agreement with the bubbles depth profile reported in figure 9. A 1st 5 nm thick layer L_1 has to be present to fit the PAS data. The positron effective diffusion length L_{d1} is only 4 nm, *S* is high ($S > S_V$) and *W* is low ($W < W_V$) respectively to the annihilation characteristics for the single vacancy (V_W) as plotted in figure 11 a. The fact that the *SW* point for L_1 is located above the V_W-$W_{lattice}$ straight line (doted line in figure 11 a representing positron annihilation in a single vacancy) indicates detection of vacancy clusters. Also, the *SW* point is far from the V_{NW} point representing positron annihilation in empty large clusters with more than 20 vacancies, i.e., in clusters with a mean diameter of approximately 1 nm. Formation of empty vacancy clusters in W under our irradiation conditions is not expected since creation of vacancy defects is mostly due to self trapping of He and trap mutation [45]. Thus, this *SW* point likely indicates vacancy clusters filled with He which should result to a decrease in *S* and an increase in *W* compared to empty vacancy clusters parameters V_{NW}. Experimental work by Bernard et al. [64] on a tungsten sample irradiated at the same helium flux and fluence but at much lower temperature of 473 K found the *SW* values being below the V_W-$W_{lattice}$ straight line clearly indicating high He/V ratio defects, i.e., He presence in the defects. It is noteworthy to notice that the *SW* value obtained in our work does not disagree with the presence of He in the vacancy clusters. The difference in *SW* in our work and in Bernard et al. [64] is due to the He/V ratio in the clusters that should be higher in on our He-irradiated sample at high temperature.

Thus, in our case such *SW* parameters describe the subsurface layer L_1 with numerous small-size defects which could be created by the He irradiation. Furthermore, numerous small-size holes were detected with the TEM imaging in the subsurface layer (figure 3 a). Lyu et al. in their recent work [65] showed that an increase of the S parameter indicates creation of nano-sized defects even when the kinetic energy of the incident He ions is below the sputtering threshold.

The 2nd L_2 and 3rd L_3 layers have thickness of 20 and 45 nm respectively. The shorter effective diffusion length in the layer L_2 is in coherence with the higher S and lower W values as compared with the parameters in the layer L_3. Such difference indicates that PAS detected more traps in the second layer than in the third which correlates with our TEM results: the largest bubbles are preferentially distributed within 10-20 nm layer below the surface (figures 3 a and 9). The SW points extracted for both layers L_2 and L_3 remain above the V_W-$W_{lattice}$ straight line indicating the detection of vacancy clusters as in L_1. But the S (resp. W) in L_2 is lower (resp. higher) than the S (resp. W) value obtained for the layer L_1. This suggests that either the size of the detected vacancy clusters is smaller in L_2 than in L_1 or that He content in the clusters is higher. TEM observations of large bubbles filled with He in the layer L_2 are in agreement with the second interpretation.

Furthermore, Pentecoste et al. [28] have shown that a peak in S (and a valley in W) parameter occurs at low positron energy with increasing He fluence. Since the size of the bubbles and their depth distribution is determined by the accumulated He concentration, in other words, by He fluence, we suggest that the peak in S (the valley in W) parameter (figure 8 a and b) can be attributed to the presence of the large overpressurized He bubbles. The results indicate that the detected vacancy defects have a large open volume with a lower density of He for L_1 than L_2.

The last layer L_4 starts below 70 nm and has characteristics of the pristine W sample. It is in correlation with the TEM observations which show very few bubbles below 70 nm in the sample (figure 9), thus, one should not expect a significant damage creation in this layer due to He irradiation.

The behavior of $S(E)$ and $W(E)$ measured in W2 is very similar to the ones in W1. Four homogeneous layers of the same thickness as in W1 were also introduced to fit the PAS data for the W2 sample. S is larger and W is smaller for W2 than for W1 indicating that the size of vacancy clusters is larger or the He content is lower in W2. The amount of helium outgassed from the sample up to 850 K ($(2.6\pm0.4)\times10^{18}\,\mathrm{He\,m^{-2}}$) is in agreement with the second interpretation [10]. Finally, the small differences in the diffusion length, S and W parameters between the samples W1 and W2 can be related with the effect of the annealing up to 850 K which may have removed a small number of He-induced defects and led to bubble shaping in the sample W2 (see TEM images in figure 3 b).

The most complex task was to find the best fit of the PAS data obtained on the sample W3. Considering the four-layers structure of the sample, a good fit is obtained for S and W parameters in the L_1 layer being close to the pristine W case while the diffusion length is much lower for W3 (59 nm against 89 nm in the pristine sample). This indicates detection of a low density of defects in the layer. The differences in the parameters obtained from the fit for the sample W3 and the W1, W2 samples may be attributed to the total volume change of detectable defects due to the recovery of the subsurface layer and a partial removal of the small He bubbles after several thermal cycling experiments up to 1350 K which is supported by the TEM observations (see figure 3 c).

The SW point extracted for the layer L_2 is on the straight line V_W-$W_{lattice}$ that could be attributed to positron annihilation in single vacancy in a first level interpretation. However, because single vacancies become mobile at a temperature above 600 K (as the migration energy of the single vacancies is $E_{V1m} = 1.66\,\mathrm{eV}$) [66] it is expected that single vacancies agglomerate in larger clusters and bubbles during the three annealing cycles up to 1350 K [29]. Since the $S_{L_2}W_{L_2}$ point is below the V_{NW}-$W_{lattice}$ line showing large empty clusters, we suggest that these S and W values correspond to the detection of He-filled vacancy clusters or bubbles which is also proven by the EELS measurements on bubbles.

Finally, the differences in the fit results for the L_2 and L_3 layers in the sample W3 compared to the W1 and W2 samples may be attributed to the decrease of the bubbles density and the change in the He density in the bubbles leading to a lower S and higher W values when He atoms number increase in a bubble of given size. This is in agreement with the shaping of the bubbles and the highest He outgassing from the W3 sample as a result of the thermal cycling experiments. Also, Lyu et al. [65] showed that implantation of D in W irradiated at high He fluence may decrease the S parameter due to the complex interplay between a formation of new defects by D implantation and the occupation of the existing defects by D atoms.

An interesting feature of the PAS results on the W3 sample is the absence of the peak and valley in the S and W parameter evolution with the positron kinetic energy (figure 8 a and b). It is related to the decrease of the density of bubbles in general and of the ones for which the He density is low.

In summary, we propose the following interpretation of defects and bubbles evolution in the He-irradiated W with thermal cycling (see figure 12). In case of the pristine sample, the positron traps are uniformly distributed within 700 nm thick layer probed by the PAS technique. The traps can be attributed to the intrinsic defects remaining after 1773 K annealing for 2 h. He irradiation results in a formation of 5 nm–thin subsurface layer with a significant number of positron traps (sample W1). This significantly damaged subsurface layer was observed with TEM technique. The positron traps in the layer or, in other words defects, might be capable of trapping hydrogen isotopes and act as a barrier for the HI trapping on He bubbles and other defects localized deeper in the sample. The largest He bubbles, preferentially distributed within 20 nm below the subsurface layer, act as weaker positron traps. Initial annealing up to 870 K (sample W2) initiates faceting of surface holes and helium bubbles in the near-surface which does not significantly affect positron annihilation characteristics in the layers. Thermal cycles up to 1350 K (sample W3) induce subsurface layer recovery (annealing of He-induced defects and smallest He bubbles), He bubbles shaping and a loss of He content. These drastic changes in the sample result in the positron annihilation

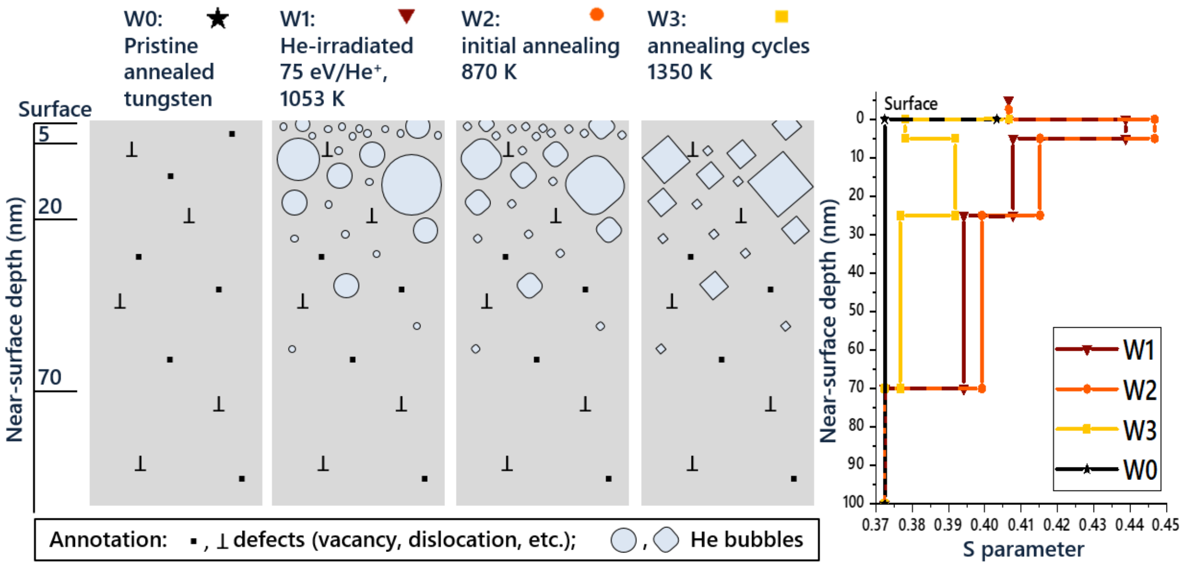

Figure 12. Schematic representation of tungsten {100} near-surface morphology evolution in our experiments.

characteristics in the 5 nm subsurface layer similar to the pristine W while PAS indicates the presence of other traps deeper in the near-surface. Thus, we can expect that HI implanted in the sample W3 can diffuse below the recovered subsurface layer and be trapped on the largest He bubbles significantly increasing HI retention in the He-irradiated W. Our new results and the presented here interpretation complement the earlier study [10] and provide more understanding on the mechanisms of the HI retention in He-irradiated tungsten.

5. Conclusions

In this work, we used an original methodology coupling scanning and transmission electron microscopy observations with positron annihilation spectroscopy to investigate effect of thermal cycling on density and shape evolution of helium bubbles in tungsten.

Our observations show that He-induced morphology changes such as holes at the surface and bubbles in the near-surface become faceted upon annealing up to 1350 K. Faceting and annealing of the surface holes are correlated with a change of surface roughness in the nanometer scale. Annealing of W above He irradiation temperature of 1053 K removed smallest (several nm in diameter) He bubbles in a 5 nm layer below the surface.

Observations of faceted He bubbles in W under different zone axes allowed to conclude on their 3D shape to be rhombic dodecahedron consisting of twelve {110} planes. This shape develops under the minimum energy requirement of the system. Moreover, the presence of a low quantity of deuterium does not play a noticeable role in holes and bubbles shaping and density evolution.

For the first time, electron energy loss spectroscopy measurements successfully revealed the presence of helium in bubbles in tungsten. He remains in the bubbles even after annealing cycles up to 1350 K. EELS measurements allowed to determine density (8.13 He nm^{-3}) and pressure (0.12 GPa) inside a bubble with diameter of 10 nm. This values agree well with the experimental data for various metals reported by Taverna [38], Frechard [39], Walsh [58], Jager [59] and a simple empirical model by Hammond [19]. A small discrepancy is mainly attributed to the decreased He content in the bubble after annealing up to 870 K. Also, one needs to develop a better numerical model relating the size of bubbles and helium content.

Positron annihilation spectroscopy study proved that thermal cycling of the He-irradiated tungsten significantly affects the density of the defects with a free volume (vacancies, clusters of vacancies, He/vacancy clusters, helium bubbles) and their depth distribution, consistently with our TEM observations. Our original study allowed to identify different layers in W depending on the defect type, density and their positron characteristics.

Successful application of the methodology on {110} surface orientation opens up an opportunity of a comparative study on other grain orientations and may help to unravel the impact of crystallographic effects on the elemental processes of implantation at low energy and diffusion of defects during high-temperature annealing. Also, *in situ* TEM cross-sectional observations on helium bubbles in tungsten during annealing may provide a better understanding of mechanisms responsible for bubbles diffusion, coalescence and rupture with respect to the bubble size and grain orientation without an impact of *ex situ* effects of oxidation and impurities, etc.

Our results on W exposed with He in laboratory conditions will also prove valuable as the post-mortem study of W actively-cooled components irradiated during the WEST tokamak operation are starting. The study will relate a more complex exposure type with fundamental characterization including the crucial impact of the temperature parameter.

Acknowledgement

The project leading to this publication has received funding from the Excellence Initiative of Aix-Marseille University - A*Midex, a French "Investissements d'Avenir" programme as well as from the ANR under grant ANR-18-CE05-0012.
This work has been also carried out within the framework of the French Federation for Magnetic Fusion Studies (FR-FCM).

References

[1] Pitts R, Carpentier S, Escourbiac F, Hirai T, Komarov V, Lisgo S, Kukushkin A, Loarte A, Merola M, Sashala Naik A, Mitteau R, Sugihara M, Bazylev B and Stangeby P 2013 *Journal of Nuclear Materials* **438** S48–S56 ISSN 0022-3115 proceedings of the 20th International Conference on Plasma-Surface Interactions in Controlled Fusion Devices URL `https://www.sciencedirect.com/science/article/pii/S0022311513000160`

[2] Sakamoto R, Bernard E, Kreter A and Yoshida N 2016 *Nuclear Fusion* **57** 016040 URL `https://doi.org/10.1088%2F1741-4326%2F57%2F1%2F016040`

[3] Sakamoto R, Bernard E, Kreter A, Martin C, Pégourié B, Pieters G, Rousseau B, Grisolia C and Yoshida N 2017 *Physica Scripta* **T170** 014062 URL `https://doi.org/10.1088%2F1402-4896%2Faa93a2`

[4] Wilson W D, Bisson C L and Baskes M I 1981 *Phys. Rev. B* **24**(10) 5616–5624 URL `https://link.aps.org/doi/10.1103/PhysRevB.24.5616`

[5] Bernard E, Sakamoto R, Tokitani M, Masuzaki S, Hayashi H, Yamada H and Yoshida N 2017 *Journal of Nuclear Materials* **484** 24 – 29 ISSN 0022-3115 URL `http://www.sciencedirect.com/science/article/pii/S0022311516306560`

[6] Ueda Y, Coenen J, De Temmerman G, Doerner R, Linke J, Philipps V and Tsitrone E 2014 *Fusion Engineering and Design* **89** 901–906 ISSN 0920-3796 proceedings of the 11th International Symposium on Fusion Nuclear Technology-11 (ISFNT-11) Barcelona, Spain, 15-20 September, 2013 URL `https://www.sciencedirect.com/science/article/pii/S0920379614001859`

[7] De Temmerman G, Bystrov K, Zielinski J J, Balden M, Matern G, Arnas C and Marot L 2012 *Journal of Vacuum Science & Technology A* **30** 041306 (*Preprint* `https://doi.org/10.1116/1.4731196`) URL `https://doi.org/10.1116/1.4731196`

[8] Doerner R, Baldwin M and Stangeby P 2011 *Nuclear Fusion* **51** 043001 URL `https://doi.org/10.1088/0029-5515/51/4/043001`

[9] Beck C E, Roberts S G, Edmondson P D and Armstrong D E J 2013 *MRS Proceedings* **1514** 99–104

[10] Ialovega M, Bernard E, Bisson R, Martin C, Sakamoto R, Kreter A, Hodille E, Angot T and Grisolia C 2020 *Physica Scripta* **T171** 014066 URL `https://doi.org/10.1088%2F1402-4896%2Fab68bd`

[11] Bernard E, Sakamoto R, Hodille E, Kreter A, Autissier E, Barthe M F, Desgardin P, Schwarz-Selinger T, Burwitz V, Feuillastre S, Garcia-Argote S, Pieters G, Rousseau B, Ialovega M, Bisson R, Ghiorghiu F, Corr C, Thompson M, Doerner R, Markelj S, Yamada H, Yoshida N and Grisolia C 2019 *Nuclear Materials and Energy* **19** 403 – 410 ISSN 2352-1791 URL `http://www.sciencedirect.com/science/article/pii/S2352179118302424`

[12] Bisson R, Hodille E, Gaspar J, Douai D, Wauters T, Gallo A, Gunn J, Hakola A, Loarer T, Nouailletas R, Morales J, Pégourié B, Reux C, Sabot R, Tsitrone E, Vartanian S, Wang E, Fedorczak N and Brezinsek S 2021 *Nuclear Materials and Energy* **26** 100885 ISSN 2352-1791 URL `https://www.sciencedirect.com/science/article/pii/S2352179120301484`

[13] ITER Organization 2018 ITER Research Plan within the Staged Approach (Level III - Provisional Version) Tech. Rep. ITR-18-003 ITER Organization accessed on 17/02/2021 URL `https://www.iter.org/technical-reports?id=9`

[14] Eckstein W, Garciá-Rosales C, Roth J and László J 1993 *Nuclear Instruments and Methods in Physics Research Section B: Beam Interactions with Materials and Atoms* **83** 95–109 ISSN 0168-583X URL `https://www.sciencedirect.com/science/article/pii/0168583X9395913P`

[15] Ziegler J F, Ziegler M and Biersack J 2010 *Nuclear Instruments and Methods in Physics Research Section B: Beam Interactions with Materials and Atoms* **268** 1818 – 1823 ISSN 0168-583X 19th International Conference on Ion Beam Analysis URL `http://www.sciencedirect.com/science/article/pii/S0168583X10001862`

[16] Hammond K D and Wirth B D 2014 *Journal of Applied Physics* **116** 143301 (*Preprint* `https://doi.org/10.1063/1.4897419`) URL `https://doi.org/10.1063/1.4897419`

[17] Maroudas D, Blondel S, Hu L, Hammond K D and Wirth B D 2016 *Journal of Physics: Condensed Matter* **28** 064004 URL `https://doi.org/10.1088%2F0953-8984%2F28%2F6%2F064004`

[18] Parish C, Hijazi H, Meyer H and Meyer F 2014 *Acta Materialia* **62** 173 – 181 ISSN 1359-6454 URL `http://www.sciencedirect.com/science/article/pii/S1359645413007301`

[19] Hammond K D, Blondel S, Hu L, Maroudas D and Wirth B D 2018 *Acta Materialia* **144** 561 – 578 ISSN 1359-6454 URL `http://www.sciencedirect.com/science/article/pii/S1359645417308315`

[20] Fan C, Li C, Parish C M, Katoh Y and Hu X 2021 *Acta Materialia* **203** 116420 ISSN 1359-6454 URL `https://www.sciencedirect.com/science/article/pii/S1359645420308375`

[21] Fan C, Katoh Y and Hu X 2021 *Nuclear Fusion* **61** 076011 URL `https://doi.org/10.1088/1741-4326/abff04`

[22] Kreter A, Brandt C, Huber A, Kraus S, Möller S, Reinhart M, Schweer B, Sergienko G and Unterberg B 2015 *Fusion Science and Technology* **68** 8–14

[23] Ferroni F, Hammond K D and Wirth B D 2015 *Journal of Nuclear Materials* **458** 419 – 424 ISSN 0022-3115 URL `http://www.sciencedirect.com/science/article/pii/S0022311514010332`

[24] Schmitz J, Litnovsky A, Klein F, Wegener T, Tan X, Rasinski M, Mutzke A, Hansen P, Kreter A, Pospieszczyk A, Möller S, Coenen J, Linsmeier C, Breuer U, Gonzalez-Julian J and Bram M 2018 *Nuclear Materials and Energy* **15** 220 – 225 ISSN 2352-1791 URL `http://www.sciencedirect.com/science/article/pii/S2352179117301023`

[25] Ialovega M 2021 *Surface Conditions of Tungsten Components: Impact on Hydrogen Inventory* Ph.D. thesis Aix-Marseille University theses.fr energie, Rayonnement, Plasma

[26] Fiji: an open-source platform for biological-image analysis | Nature Methods URL `https://www.nature.com/articles/nmeth.2019`

[27] Desgardin P, Liszkay L, Barthe M F, Henry L, Briaud J L, Saillard M, Lepolotec L, Corbel C, Blondiaux G, Colder A, Marie P and Levalois M 2001 *Materials Science Forum* **363-365** 523 – 525

[28] Pentecoste L, Thomann A L, Brault P, Lecas T, Desgardin P, Sauvage T and Barthe M F 2017 *Acta Materialia* **141** 47–58 ISSN 1359-6454 URL `https://www.sciencedirect.com/science/article/pii/S1359645417307310`

[29] Lhuillier P E, Barthe M F, Desgardin P, Egger W and Sperr P 2009 *physica status solidi c* **6** 2329–2332 (*Preprint* `https://onlinelibrary.wiley.com/doi/pdf/10.1002/pssc.200982114`) URL `https://onlinelibrary.wiley.com/doi/abs/10.1002/pssc.200982114`

[30] Hollingsworth A, Barthe M F, Lavrentiev M Y, Derlet P, Dudarev S, Mason D, Hu Z, Desgardin P, Hess J, Davies S, Thomas B, Salter H, Shelton E, Heinola K, Mizohata K, De Backer A, Baron-Wiechec A, Jepu I, Zayachuk Y, Widdowson A, Meslin E and Morellec A 2022 *Journal of Nuclear Materials* **558** 153373 ISSN 0022-3115 URL `https://www.sciencedirect.com/science/article/pii/S0022311521005936`

[31] Troev T, Popov E, Staikov P, Nankov N and Yoshiie T 2009 *Nuclear Instruments and Methods in Physics Research Section B: Beam Interactions with Materials and Atoms* **267** 535–541 ISSN 0168-583X URL `https://www.sciencedirect.com/science/article/pii/S0168583X08013190`

[32] Xu Q, Ishizaki T, Sato K, Yoshiie T and Nagata S 2006 *MATERIALS TRANSACTIONS* **47** 2885–2887

[33] Suslova A, El-Atwani O, Sagapuram D, Harilal S S and Hassanein A 2014 *Scientific Reports* **4** 6845 ISSN 2045-2322 URL `https://doi.org/10.1038/srep06845`

[34] Sefta F, Juslin N and Wirth B D 2013 *Journal of Applied Physics* **114** 243518 (*Preprint* `https://doi.org/10.1063/1.4860315`) URL `https://doi.org/10.1063/1.4860315`

[35] Gatan 2020 *EELS atlas* (eels.info) URL `https://eels.info/atlas`

[36] Iakoubovskii K, Mitsuishi K, Nakayama Y and Furuya K 2008 *Microscopy Research and Technique* **71** 626–631 (*Preprint* `https://analyticalsciencejournals.onlinelibrary.wiley.com/doi/pdf/10.1002/jemt.20597`) URL `https://analyticalsciencejournals.onlinelibrary.wiley.com/doi/abs/10.1002/jemt.20597`

[37] Potin V, Cacucci A and Martin N 2017 *Micron* **101** 62–68 ISSN 0968-4328 URL `https://www.sciencedirect.com/science/article/pii/S0968432817301063`

[38] Taverna D, Kociak M, Stéphan O, Fabre A, Finot E, Décamps B and Colliex C 2008 *Phys. Rev. Lett.* **100**(3) 035301 URL `https://link.aps.org/doi/10.1103/PhysRevLett.100.035301`

[39] Frechard S, Walls M, Kociak M, Chevalier J, Henry J and Gorse D 2009 *Journal of Nuclear Materials* **393** 102 – 107 ISSN 0022-3115 URL

`http://www.sciencedirect.com/science/article/pii/S0022311509006345`

[40] van Veen A, Schut H, Clement M, de Nijs J, Kruseman A and IJpma M 1995 *Applied Surface Science* **85** 216–224 ISSN 0169-4332 proceedings of the Sixth International Workshop on Slow-Positron Beam Techniques for Solids and Surfaces URL `https://www.sciencedirect.com/science/article/pii/0169433294003343`

[41] Nishijima D, Ye M, Ohno N and Takamura S 2004 *Journal of Nuclear Materials* **329-333** 1029 – 1033 ISSN 0022-3115 proceedings of the 11th International Conference on Fusion Reactor Materials (ICFRM-11) URL `http://www.sciencedirect.com/science/article/pii/S0022311504002934`

[42] Kajita S, Sakaguchi W, Ohno N, Yoshida N and Saeki T 2009 *Nuclear Fusion* **49** 095005 URL `https://doi.org/10.1088%2F0029-5515%2F49%2F9%2F095005`

[43] Wilson W D 1983 *Radiation Effects* **78** 11–24 (*Preprint* `https://doi.org/10.1080/00337578308207356`) URL `ttps://doi.org/10.1080/00337578308207356`

[44] Sefta F, Hammond K D, Juslin N and Wirth B D 2013 *Nuclear Fusion* **53** 073015 URL `https://doi.org/10.1088%2F0029-5515%2F53%2F7%2F073015`

[45] Boisse J, Domain C and Becquart C 2014 *Journal of Nuclear Materials* **455** 10–15 ISSN 0022-3115 proceedings of the 16th International Conference on Fusion Reactor Materials (ICFRM-16) URL `https://www.sciencedirect.com/science/article/pii/S0022311514001032`

[46] Delaporte-Mathurin R, Ialovega M, Hodille E A, Mougenot J, Charles Y, Bernard E, Martin C and Grisolia C 2021 *Scientific Reports* **11** 14681 ISSN 2045-2322 URL `https://doi.org/10.1038/s41598-021-93542-9`

[47] Hamid A Y, Sun J, Zhang H, Jadon A S and Stirner T 2019 *Computational Materials Science* **163** 141–147 ISSN 0927-0256 URL `https://www.sciencedirect.com/science/article/pii/S0927025619301314`

[48] Kempshall B W, Schwarz S M, Prenitzer B I, Giannuzzi L A, Irwin R B and Stevie F A 2001 *Journal of Vacuum Science & Technology B: Microelectronics and Nanometer Structures Processing, Measurement, and Phenomena* **19** 749–754 (*Preprint* `https://avs.scitation.org/doi/pdf/10.1116/1.1368670`) URL `https://avs.scitation.org/doi/abs/10.1116/1.1368670`

[49] Xu Q, Yoshiie T and Huang H 2003 *Nuclear Instruments and Methods in Physics Research Section B: Beam Interactions with Materials and Atoms* **206** 123 – 126 ISSN 0168-583X 13th International Conference on Ion Beam Modification of Materials URL `http://www.sciencedirect.com/science/article/pii/S0168583X03006979`

[50] El-Atwani O, Hattar K, Hinks J, Greaves G, Harilal S and Hassanein A 2015 *Journal of Nuclear Materials* **458** 216–223 ISSN 0022-3115 URL `https://www.sciencedirect.com/science/article/pii/S0022311514010472`

[51] El-Atwani O, Cunningham W, Perez D, Martinez E, Trelewicz J, Li M and Maloy S 2020 *Scripta Materialia* **180** 6–10 ISSN 1359-6462 URL `https://www.sciencedirect.com/science/article/pii/S1359646220300282`

[52] Ohno N, Hirahata Y, Yamagiwa M, Kajita S, Takagi M, Yoshida N, Yoshihara R, Tokunaga T and Tokitani M 2013 *Journal of Nuclear Materials* **438** S879 – S882 ISSN 0022-3115 proceedings of the 20th International Conference on Plasma-Surface Interactions in Controlled Fusion Devices URL `http://www.sciencedirect.com/science/article/pii/S0022311513001980`

[53] Dürrschnabel M, Klimenkov M, Jäntsch U, Rieth M, Schneider H C and Terentyev D 2021 *Scientific Reports* **11** 7572 ISSN 2045-2322 URL `https://doi.org/10.1038/s41598-021-86746-6`

[54] Wei Q, Li N, Sun K and Wang L 2010 *Scripta Materialia* **63** 430 – 433 ISSN 1359-6462 URL `http://www.sciencedirect.com/science/article/pii/S135964621000299X`

[55] Goodhew P J and Tyler S K 1981 *Proceedings of the Royal Society of London. Series A, Mathematical and Physical Sciences* **377** 151–184 ISSN 00804630 URL `http://www.jstor.org/stable/2397037`

[56] Huang X, Lv C and Chu H 2021 *Scientific Reports* **11** 830 ISSN 2045-2322 URL

`https://doi.org/10.1038/s41598-020-80167-7`

[57] Haghighat S M H, Lucas G and Schaublin R 2009 *EPL (Europhysics Letters)* **85** 60008 URL `https://doi.org/10.1209%2F0295-5075%2F85%2F60008`

[58] Walsh C A, Yuan J and Brown L M 2000 *Philosophical Magazine A* **80** 1507–1543 (*Preprint* `https://doi.org/10.1080/01418610008212134`) URL `https://doi.org/10.1080/01418610008212134`

[59] Jäger W, Manzke R, Trinkaus H, Crecelius G, Zeller R, Fink J and Bay H 1982 *Journal of Nuclear Materials* **111-112** 674–680 ISSN 0022-3115 URL `https://www.sciencedirect.com/science/article/pii/0022311582902884`

[60] Pyper N C, Naginey T C, Nellist P D and Whelan C T 2017 *Philosophical Magazine Letters* **97** 295–303 (*Preprint* `https://doi.org/10.1080/09500839.2017.1347724`) URL `https://doi.org/10.1080/09500839.2017.1347724`

[61] Lucas A 1984 *Physica B+C* **127** 225–239 ISSN 0378-4363 proceedings of the 4th General Conference of the Condensed Matter Division of the EPS URL `https://www.sciencedirect.com/science/article/pii/S0378436384800352`

[62] Vehanen A, Lynn K G, Schultz P J and Eldrup M 1983 *Applied Physics A* **32** 163–167 ISSN 1432-0630 URL `https://doi.org/10.1007/BF00616613`

[63] Hautojärvi P and Corbel C 1995 *Proceedings of the International School of Physics "Enrico Fermi"* **125** 491–532 ISSN 0074-784X URL `https://doi.org/10.3254/978-1-61499-211-0-491`

[64] Bernard E, Sakamoto R, Kreter A, Barthe M F, Autissier E, Desgardin P, Yamada H, Garcia-Argote S, Pieters G, Chêne J, Rousseau B and Grisolia C 2017 *Physica Scripta* **T170** 014023 URL `https://doi.org/10.1088/1402-4896/aa89f7`

[65] Lyu Y M, Xu Y P, Li X C, Shen X, Wu B Y, Yip C S, Gao X, Lin X D, Yang Z S, Cao X Z, Zhou H S and Luo G N 2021 *Nuclear Materials and Energy* **29** 101094 ISSN 2352-1791 URL `https://www.sciencedirect.com/science/article/pii/S2352179121001605`

[66] Becquart C and Domain C 2007 *Nuclear Instruments and Methods in Physics Research Section B: Beam Interactions with Materials and Atoms* **255** 23–26 ISSN 0168-583X computer Simulation of Radiation Effects in Solids URL `https://www.sciencedirect.com/science/article/pii/S0168583X06010585`